Production of long bunch trains with 4.5 μC total charge using a photoinjector

Oznur Mete,[1,2,*] Eric Chevallay,[1] Marta Csatari,[1,3] Anne Dabrowski,[1] Steffen Doebert,[1] Daniel Egger,[1,2]
Valentine Fedosseev,[1] Maja Olvegaard,[1] and Massimo Petrarca[1,4]

[1]*European Organization for Nuclear Research, 1211 Geneva, Switzerland*
[2]*EPFL, 1015 Lausanne, Switzerland*
[3]*Paul Scherrer Institut, 5232 Villigen, Switzerland*
[4]*University of Geneva, 1211 Geneva, Switzerland*
(Received 30 August 2011; published 17 February 2012)

A photoinjector, PHIN (PHotoINjector), has been realized at CERN by a joint effort of several institutes within the European Coordinated Accelerator Research in Europe program. The test facility has been installed and commissioned at CERN with the aim to demonstrate the beam parameters needed for the CLIC Test Facility 3 (CTF3). This beam is unique with respect to its long bunch train and high average charge per bunch requirements. The nominal beam for CTF3 consists of 1908 bunches each having a 2.33 nC charge and a bunch frequency of 1.5 GHz. Thus, a total charge of ~4.4 μC has to be extracted and accelerated. The stability of the intensity and the beam parameters along this exceptionally high average current train is crucial for the correct functioning of the CLIC drive beam scheme. Consequently, extensive time-resolved measurements of the transverse and longitudinal beam parameters have been developed, optimized, and performed. The shot-to-shot intensity stability has been studied in detail for the electron and the laser beams, simultaneously. The PHIN photoinjector has been commissioned between 2008 and 2010 during intermittent operations. This paper reports on the obtained results in order to demonstrate the feasibility and the stability of the required beam parameters.

I. INTRODUCTION

The Compact Linear Collider (CLIC) study proposes a multi-TeV, high luminosity, electron-positron linear collider in order to fulfill the current desire for a lepton collider [1,2]. For a high energy linear accelerator, such as CLIC, the length of the machine is an important item to be optimized in terms of the cost effectiveness. Within the CLIC study, an rf system has been proposed which uses normal conducting accelerating cavities operating at 12 GHz with a nominal accelerating gradient of 100 MV/m to accelerate the beams with an rf pulse length of 239 ns. An innovative scheme of high peak rf power production for the high accelerating gradient has been proposed for CLIC. The so-called "two-beam acceleration scheme" consists of two types of beams that are running parallel to each other. The first type includes the e^- and e^+ beams to be accelerated for the collision experiments and is called "the main beam." The second type of beam in the CLIC scheme is "the drive beam" and will be employed for the rf power production. The quality of the main beam

acceleration depends on the stability of the power generated by the drive beam. Therefore, the optimization of the drive beam production with the proper time structure and within the required beam dynamics tolerances is one of the most important accelerator physics aspects of the project.

Currently in the conceptual level, the baseline design of the drive beam injector relies on a thermionic gun [3]. Because of the drive beam time structure specifications, the injector should generate a beam with empty rf buckets within successive bunches. This has been provided by using subharmonic bunchers. However, a percentage of electrons (4%–5%) is trapped in the empty buckets and form the so-called "satellite bunches" in between the "main bunches" due to the subharmonic bunching system. This unwanted parasitic charge has to be removed by means of the magnetic chicanes or rf deflectors to prevent the degradation in power generation. This procedure might cause a total beam intensity loss of up to 20%.

Under these circumstances, it is prudent to consider a photoinjector alternative to the existing thermionic gun.

A photoinjector is an electron source that uses laser induced photoemission of electrons from the surface of a metallic or a semiconductor cathode. It provides a compact, high charge, low emittance electron beam. The system is compact since it does not require an additional bunching system. The time structure of the electron beam is provided by manipulating the time structure of the laser

*Corresponding author.
oznur.mete@cern.ch

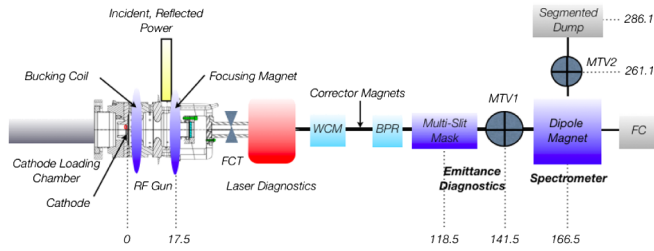FIG. 1.   The layout of the PHIN photoinjector.

FIG. 2.   The schematic layout of the laser system for PHIN.

pulses. Therefore the production of the parasitic charge is not an issue for photoinjectors.

II. PHIN PHOTOINJECTOR

The photoinjector research and development activity, PHIN, is a part of the Coordinated Accelerator Research in Europe (CARE) program. Part of this research program is devoted to exploring the possibility of replacing the thermionic gun originally proposed to produce the CLIC drive beam, with a photoinjector.

The PHIN photoinjector [4,5] consists of a Cs_2Te photocathode, a laser system, a $2 + 1/2$ cell rf gun and a set of solenoids for focusing. The test-stand at CERN also houses a section with various instruments to measure the transverse and the longitudinal beam parameters with different techniques. The layout of the setup is shown in Fig. 1. The specifications of the PHIN photoinjector is presented in Table I.

Laser.—The laser architecture is a master oscillator that is followed by two power amplifiers running in steady-state

TABLE I.   The specifications for the PHIN photoinjector.

Parameter	Specification
Laser	
UV laser pulse energy (nJ)	370
Micropulse repetition rate (GHz)	1.5
Macropulse repetition rate (Hz)	1–5
Train length (ns)	1273
Electron beam	
Charge per bunch (nC)	2.33
Charge per train (nC)	4446
Bunch length (ps)	8
Current (A)	3.5
Transverse normalized emittance (mm mrad)	<25
Energy spread (%)	<1
Energy (MeV)	5.5
Charge stability (%, rms)	<0.25
rf gun	
rf gradient (MV/m)	85
rf frequency (GHz)	2.99855
Cathode	Cs_2Te
Quantum efficiency (%)	3

saturation. The schematic layout of the laser system is presented in Fig. 2. A commercial Nd:YLF oscillator produces a continuous train of pulses at 1.5 GHz repetition rate which is synchronized to the rf of the machine with an accuracy better than 500 fs. Afterwards, its power is boosted by a preamplifier to 10 W (6.6 nJ/pulse). This is followed by two high power burst mode, side pumped, rod amplifiers, AMP1 and AMP2. These amplifiers have been designed at Rutherford Appleton Laboratory and reconstructed at CERN [6]. They operate in steady-state saturation and deliver 8.3 kW pulse train mean power (5.5 mJ/pulse) with the current configuration [7]. A fast Pockels cell with 3 ns rise and fall time creates the macropulse time structure for the experiment. CTF3 requires a ~1.270 μs long train of 1.5 GHz pulses with 1–5 Hz burst repetition rate. However, the system is very versatile and can provide long 140 ms trains with up to 50 Hz repetition rate, required for future CLIC drive beam. The Cs_2Te cathode requires UV for photoemission, so two second harmonic stages were installed in collaboration with CEA Saclay (France) and IAP Nizhny Novgorod (Russia) to generate the pulses at 262 nm. The beam shaping and its transport to the cathode is done with a relay system which allows beam size changes within a range of 0.5–2.5 mm (1σ). The beam is delivered to the cathode with an energy of up to 370 nJ and in 6.5 ps (FWHM) long Gaussian pulses.

Radio-frequency gun.—The laser-driven PHIN rf gun consists of a $2 + 1/2$ cell normal conducting S-band standing wave cavity. The gun was designed by Laboratoire de l'Accélérateur Linéaire and based on a previous CERN design [8]. It has been optimized for the high charge by choosing an angle of 3.4° to the half-cell wall, around the photocathode, to provide additional transverse focusing with an rf gradient of 85 MV/m. Additionally, the shape of the iris was changed from circular to elliptical to decrease the surface electric field and therefore minimize the electrical breakdown and dark current levels. The design of the rf gun aims to maximize the vacuum pumping speed which improves the dynamic vacuum and, therefore, the photocathode operating lifetime. Therefore, a nonevaporable getter (NEG) thin film has been implemented on the wall of the antichamber that is placed around the cavity. However, the NEG has not been activated so far.
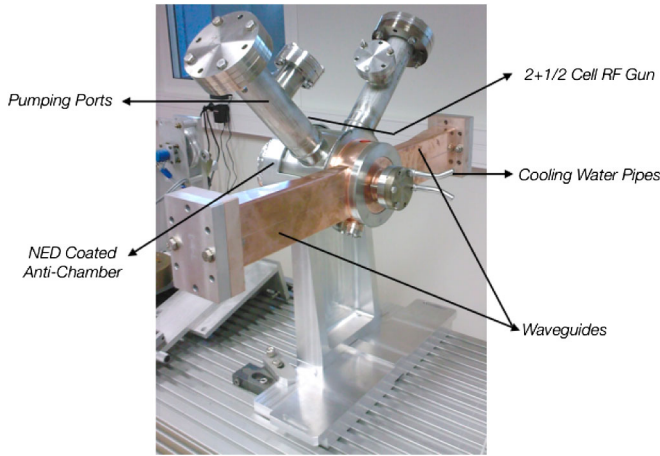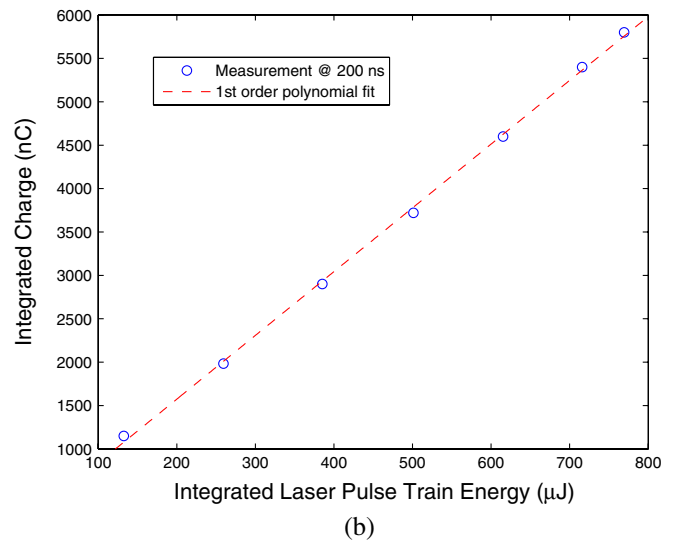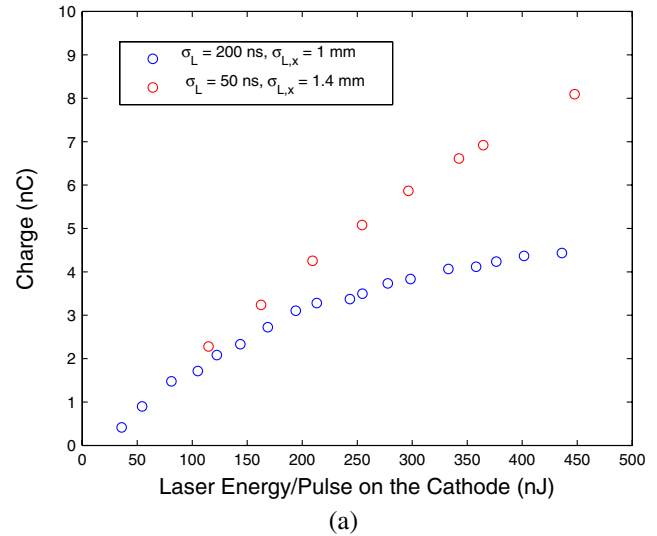
FIG. 3. The PHIN rf gun.

(a)

(b)

FIG. 4. (a) Photoinjector charge yield per bunch with the increasing laser pulse energy for different laser spot sizes and train lengths denoted by $\sigma_{L,x}$ and σ_L, respectively. (b) The linear behavior of the photoinjector in terms of the integrated charge and the laser energy over the pulse train.

A photograph of the PHIN rf gun is shown in Fig. 3. The π resonance mode is used for the acceleration in the PHIN rf gun which corresponds to a frequency of 2.998 55 GHz.

III. CHARGE PRODUCTION

Charge measurements were done by using either a fast current transformer (FCT) or a Faraday cup (FC) installed in the setup. For most of the charge measurements, the FCT was preferred due to its location after the rf gun, but the FC is the most useful to study the charge transmission along the beam line.

The charge production characteristics have been studied, systematically, during the PHIN commissioning. In principle, the amount of the charge produced by the photoemission increases linearly with the laser energy per pulse. In Fig. 4(a), a charge measurement is presented in order to demonstrate this behavior. The measurement reveals a region where the charge yield increases linearly with the laser energy per pulse. This linear region continues up to energies of 200 nJ. At a certain point the slope of the curve decreases and finally the increment converges to a maximum extractable charge value. This region is called the "saturation region." During these studies, a bunch train of 200 ns was measured. A maximum charge yield of 4.4 nC per bunch has been achieved for a laser spot size of ~1 mm (1σ), even exceeding the PHIN specification of 2.33 nC per bunch. Producing a high amount of charges per bunch for the 1200 ns long bunch train is one of the future goals of the activity in order to achieve the required high average current. According to Eq. (1) [9], the maximum achievable charge per bunch is 4.7 nC at a gradient of 85 MV/m and a laser spot size of 1 mm. The experimental value agrees well with the theoretical limit. Similar measurements were performed with a larger laser spot size of 1.4 mm in order to increase the charge yield. Consequently, a charge yield of 8.1 nC per bunch has been achieved for a short bunch train of 50 ns:

$$Q[\text{nC}] = \frac{E_{\text{acc}}[\text{MV/m}]\sigma_x^2[\text{mm}^2]}{18}. \tag{1}$$

In addition, the saturation of the photoemission has been shown to be an effect related to the space charge effect during emission of charge per single pulse [10]. The total charge production with a long train of these pulses is shown to be independent of this saturation. This can be better seen in accordance with the measurement shown in Fig. 4(b). For this measurement, the laser spot size was adjusted to 1 mm, the laser micropulse energy was kept constant at 420($\pm$17) nJ, whereas the length of the laser train was increased, systematically. During the measurement, no saturation has been observed in the charge per
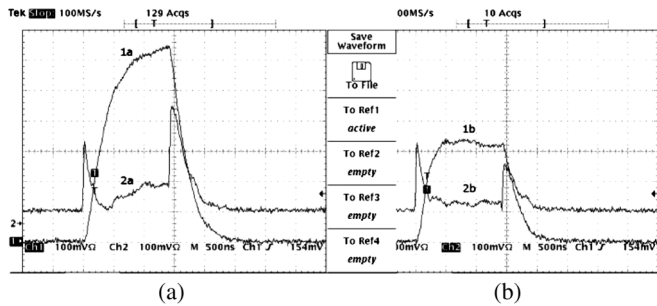
FIG. 5.   Beam loading compensation. (a) rf power in the gun (1a) and reflected power (2a) when no beam is present. (b) rf power in the gun (1b) and reflected power (2b) when the beam is present.

train as a function of the increasing integrated laser pulse train energy.

IV. BEAM LOADING COMPENSATION

The electron beam is accelerated in the rf field provided by the PHIN rf gun. During the acceleration the beam absorbs energy from the rf field. This beam loading has to be compensated in order to provide a constant accelerating gradient inside the rf cavity.

The beam loading compensation is studied and optimized for the PHIN photoinjector by adjusting the timing of the beam versus the rf pulse. The measured rf power and its reflection are shown in Fig. 5(a) when there is no beam and in 5(b) the beam is present. In the presence of the beam, an rf pulse shape has been optimized resulting in a beam energy stability better than 1%. The signals of the reflection show that the cavity is matched to the beam loading case as optimized in the design (see Sec. II). One has to note that the timing has to be adjusted for different bunch charges in order to provide the adequate compensation. The measurements have been performed after the optimization of the beam loading for the rest of the commissioning, especially for the long trains of 1.2 μs.

V. BEAM DYNAMICS MEASUREMENTS AND SIMULATIONS

During the PHIN commissioning, systematic measurements and simulations have been done in order to characterize the transverse and longitudinal beam parameters. The stability and the tolerances of the injector have been studied. The variation of the system variables such as the laser and the rf power have been investigated in order to specify the correlation between these variables and the electron beam. The measurements have been simulated with respect to the photoinjector model by using PARMELA [11]. The basic systematic measurement and simulation results on the PHIN photoinjector are presented

in this section. One can refer to Ref. [12] for the complete report on the commissioning of the PHIN photoinjector.

A. Transverse phase space measurement with a multislit mask

The beam size and the transverse normalized emittance measurements have been performed, in the context of the transverse phase space studies for PHIN. The slit mask provides 25 slits and each slit has an opening of 100 μm, a center-to-center distance of 900 μm. The distance between the multislit mask and the beamlet observation screen is fixed to 23 cm. The optical transition radiation (OTR) profiling technique has been used for monitoring of the beamlets on the observation screen.

The emittance has been measured by introducing a multislit mask within the vacuum chamber in front of the incoming beam. The details of the emittance analysis method are explained in [13].

A typical horizontal beam intensity profile after a multislit mask, with subsequent slits along the horizontal axis, is presented in Fig. 6. In this method, the transverse geometric emittance, ε, can be calculated by using the formula given in Eq. (2) [14],

$$\varepsilon = \sqrt{\frac{\left(\sum_{i=1}^{N} \rho_i x_i^2\right)\left(\sum_{j=1}^{N} \rho_j x_j'^2\right) - \left(\sum_{i=1}^{N} \rho_i x_i x_i'\right)^2}{\left(\sum_{i=1}^{N} \rho_i\right)^2}}, \quad (2)$$

where x_i and x_i' are the position and the divergence of the ith beamlet, respectively. The intensity of each beamlet is denoted by ρ_i.

In Fig. 7, the transverse normalized emittance has been measured as a function of the focusing solenoid current for laser spot sizes of 2 and 4 mm. The laser spot size is defined
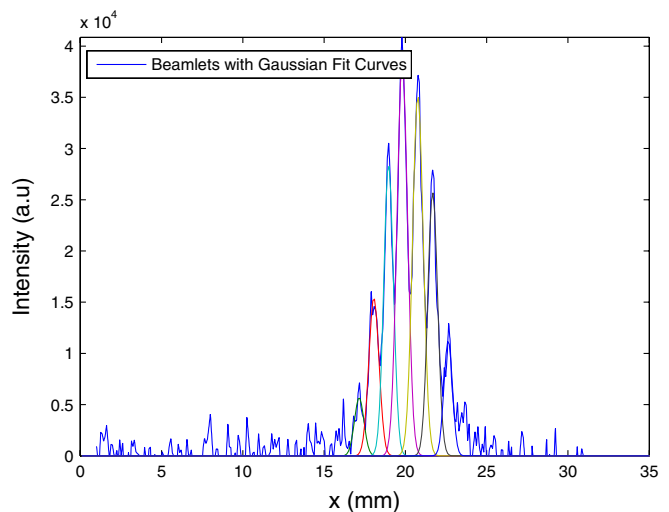

FIG. 6.   Beam profile after the multislit mask, with Gaussian fit curves for individual beamlets.
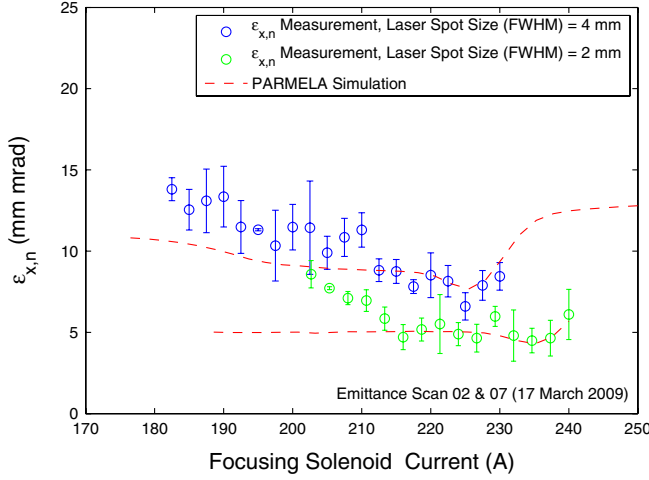
FIG. 7. Emittance measurement with respect to the laser spot size: (blue) $\sigma_{laser} = 4$ mm, $Q = 1.28$ nC, $E = 5.5$ MeV, train length $= 200$ ns; (green) $\sigma_{laser} = 2$ mm, $Q = 1.1$ nC, $E = 5.7$ MeV, train length $= 200$ ns.

as the region containing 85% of the light. The laser spot size is one of the inputs to PARMELA in order to initiate the beam properties. The 1σ values of the laser spot sizes used in the simulations are 0.8 and 1.6 mm. The compensation of the space charge induced beam emittance was achieved for both conditions at different focusing solenoid currents. At these particular solenoid settings where the minimum occurs, the emittance is 6.6 and 4.5 mm mrad while the laser spot is 4 and 2 mm, respectively. The measurement agrees with the simulations within the statistical error ranges for the higher solenoid currents. Although the two measurements were performed in different days, the charge per bunch and the energy of the beam have been maintained as close as possible for each case. It has been experimentally shown that the emittance scales with the laser spot size as expected.

In addition, each emittance curve in Fig. 7 demonstrates a very important phenomenon called the emittance compensation. For high-brightness beams the space charge force is a function of the longitudinal position within the bunch. This can be approached analytically by considering a single bunch sliced along the longitudinal axis [15,16]. Therefore the measured emittance can be seen as a projection of the emittances of these individual slices. The transverse normalized emittance can be minimized when all the slices in the transverse phase space line up in the presence of proper focusing. For the PHIN setup, the focusing has been provided by the magnetic field generated by a solenoid. Once it is determined, the focusing magnet current can be fixed in order to provide the minimum emittance. The focusing must be readjusted in accordance with different operational conditions and beam parameters. For example, in this measurement, the emittance minimum occurs at 225 A when the laser spot size is 4 mm, whereas it shifts to 235 A for the spot size of 2 mm.

1. Systematic error analysis

The appropriate error calculations have been included within the emittance measurement analysis. An expression has been derived for the systematic error calculations of the transverse emittance measurement by using the standard error propagation:

$$
\sigma_\varepsilon^2 = \frac{(\rho_j x_j'^2)^2 (4\rho_i^2 x_i^2 \sigma_{x_i}^2 + x_i^4 \sigma_{\rho_i}^2)}{4\varepsilon^2 \left(\sum_{i=1}^N \rho_i\right)^4}
$$
$$
+ \frac{(\rho_j x_j^2)^2 (4\rho_i^2 x_i'^2 \sigma_{x_i'}^2 + x_i'^4 \sigma_{\rho_i}^2)}{4\varepsilon^2 \left(\sum_{i=1}^N \rho_i\right)^4}
$$
$$
+ \frac{(\rho_i^2 x_i'^2 \sigma_{x_i}^2 + \rho_i^2 x_i^2 \sigma_{x_i'}^2 + x_i^2 x_i'^2 \sigma_{\rho_i}^2)(\rho_i x_i x_i')^2}{\varepsilon^2 \left(\sum_{i=1}^N \rho_i\right)^4}
$$
$$
- \frac{2(\sum_{i=1}^N \rho_i x_i^2)(\sum_{j=1}^N \rho_j x_j'^2)(\sum_{i=1}^N \rho_i x_i x_i')^2(\sum_{i=1}^N \sigma_{\rho_i}^2)}{\varepsilon^2 (\sum_{i=1}^N \rho_i)^6}
$$
$$
+ \frac{\varepsilon^2 (\sum_{i=1}^N \sigma_{\rho_i}^2)}{(\sum_{i=1}^N \rho_i)^6}. \tag{3}
$$

This expression is given in Eq. (3) in terms of the first moment, second moment, and the intensities of the beamlets as well as the individual errors on these observables. The errors on the observables, used in the calculations, are given in Table II. The slit spacing and the distance between the multislit mask and the observation screen have been used to determine the errors on the beamlet positions and divergences. Additionally, the shot-to-shot intensity stability of the beam was taken into account.

Further systematic errors may originate from the background subtraction method of the OTR profiles, non-Gaussian intensity distribution of the beamlets close to the emittance minimum, and underestimation of the beam size for the beamlets at the tails of the profile with low signal to noise ratios. However, the contributions from those sources have not been included in the analysis.

The systematic errors have been calculated for the emittance measurement shown in Fig. 8. The figure shows a comparison between the systematic and the statistical error

TABLE II. The errors on the position and the divergence of the beamlets have been calculated in terms of the slit width and the mask-screen distance. The error on the beamlet intensities has been calculated as the product of the measured relative intensities of the individual beamlets, ρ_i, and the average electron beam intensity stability, ρ_b, during the measurement.

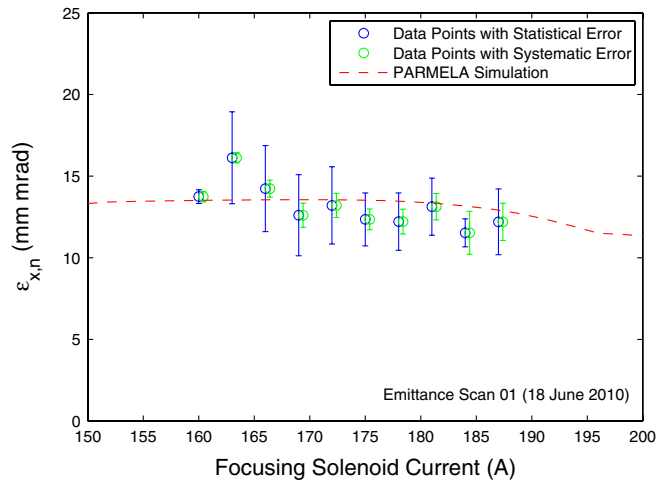| Parameter	Value
Error on the mean position, σ_x [mm]	0.01
Error on the beam divergence, $\sigma_{x'}$ [mrad]	0.4
Error on the beamlet intensities, σ_ρ [a.u.]	$\rho_b \times \rho_i$

FIG. 8. The comparison of the statistical and the systematic errors on the multislit method for the emittance scan as a function of the focusing.
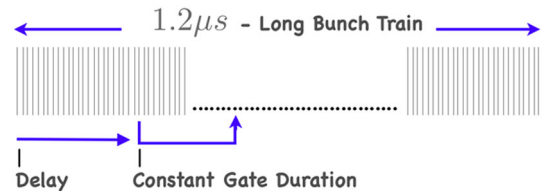

FIG. 9. The illustration of the time-resolved OTR profiling of the electron beam. The scheme as shown in the figure would allow a measurement that is integrated over a region determined by the constant gate duration.

on each measured point. Each data point represents an average of five subsequent measurements. The statistical error on each point is the statistical uncertainty of the subsequent measurements. The systematic error of each data point has been found by propagation of the systematic errors of each subsequent measurement.

The measurement indicates that the systematic and the statistical errors are comparable. Nevertheless, the systematic error for the measurement is less than the statistical deviations, for this particular example which confirms the reliability of the measurement setup within the available statistics and the systematic uncertainties under consideration. Indeed, the statistical errors indicate shot-to-shot beam fluctuations. The shot-to-shot stability is an important aspect of the photoinjector systems. The multislit emittance measurement method is rather suitable for these systems for its single-shot acquisition property.

2. Time-resolved measurement of the transverse phase space

The multislit emittance measurement setup can be upgraded with an intensified-gated CCD camera to perform time-resolved emittance measurements along the bunch train. A camera with an adjustable gate duration from 100 ns to several milliseconds was used for the measurements on the PHIN beam. The camera was triggered by an external signal synchronized to the laser timing. One can delay the camera timing with respect to the laser timing in order to monitor a particular duration of the bunch train. For these measurements, the camera gate can be adjusted according to the required time resolution, and the specification of the CCD camera, as illustrated in Fig. 9. For each subsequent measurement point, the camera gate delay is increased in order to snapshot a different longitudinal

position along the pulse train. During the commissioning of the long electron pulse train, a beam of a 1.2 or 1.3 μs was provided for the measurements. The beam size, emittance, and energy of the beam were measured in a time-resolved manner.

Figure 10(a) shows the beam size measurements as a function of the focusing current. The data points with different colors, at a particular focusing solenoid setting, represent the time-resolved measurements for this setting as a function of the gate position with the steps of 200 ns. Figure 10(b) shows the details of a measurement at a particular magnet setting. A stable beam with a charge per bunch of 1.4 nC at an energy of 4.9 MeV has been provided for these time-resolved solenoid scans. The measurement agrees very well with the simulation within the measured statistical error ranges.

In a similar way, Fig. 11 presents the results of an emittance measurement with a 1.2 μs beam of 1.6 nC per bunch at 4.8 MeV. The emittance has been measured in the beginning, in the middle, and in the end of the bunch train, i.e., with steps of 400 ns. The focusing solenoid current has been changed systematically during the measurement. According to the measurement the emittance compensation can be achieved by a focusing provided by a solenoid current of 206.7 A. The data point where this minimum occurs is shown in detail in Fig. 12. The average transverse normalized emittance has been measured as 9.45 mm mrad with a fluctuation of 9.4% along the pulse train.

The time-resolved emittance measurement can be performed with shorter gate durations in order to increase the resolution along the train. Such a measurement is shown in Fig. 13. Time-resolved emittance measurements reveal an oscillationlike behavior that is refining with the increasing resolution along the train. The variations in the rf field and the laser intensity profile are the most probable sources of fluctuation. Therefore, the inheritance of the instabilities from these sources should be studied. Consequently, further investigations have been done in pursuit of a correlation between the rf field and the beam parameters. Figure 13 shows the fluctuation of the emittance along the bunch train in comparison with the rf pulse shape. According to this particular measurement an average rf power fluctuation of 1% and an average emittance
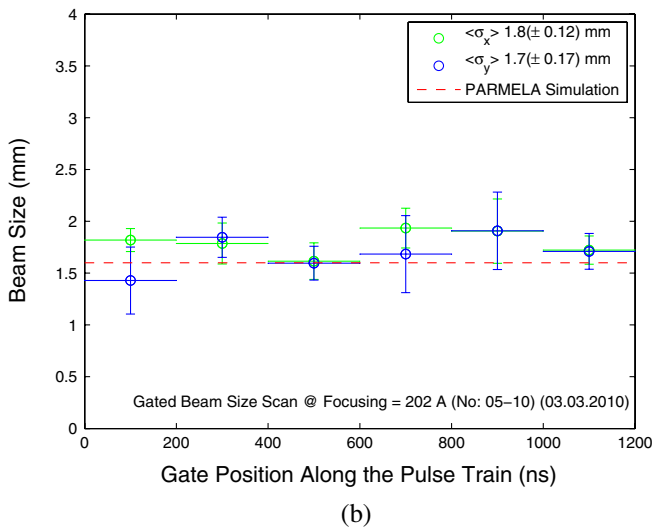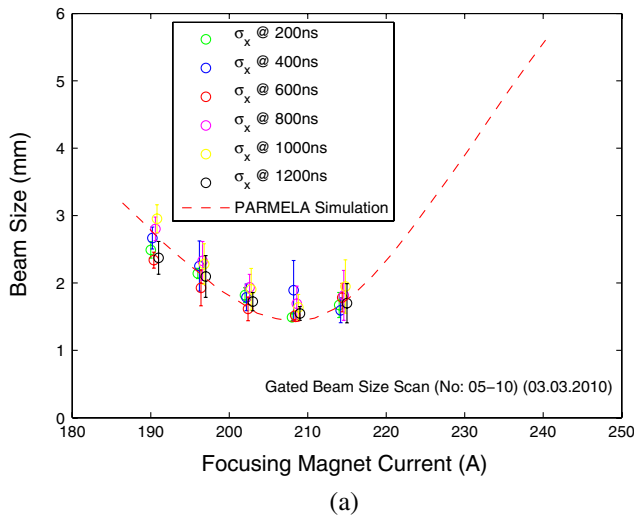
(a)

(b)

FIG. 10. Beam size scan along the bunch train for a beam of 1.4 nC, 4.9 MeV. (a) Horizontal beam size scan as a function of the focusing. (b) Representation of the measurement under a focusing current of 202 A as a function of the gate position.
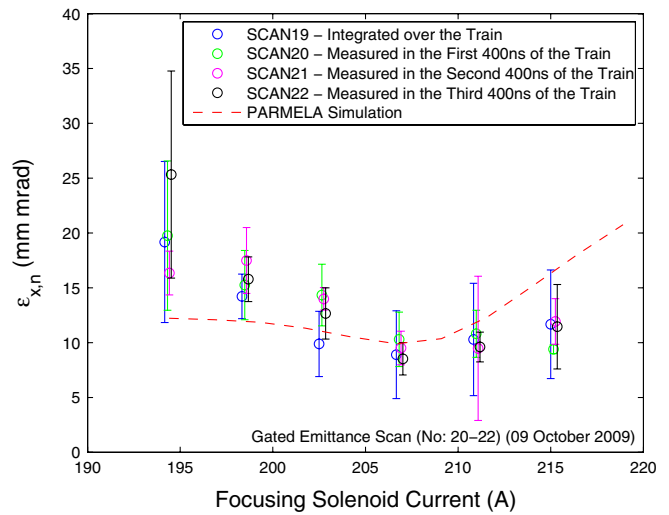

FIG. 11. Emittance scan, with a beam of 1.6 nC, 4.8 MeV, along the bunch train with the steps of 400 ns.
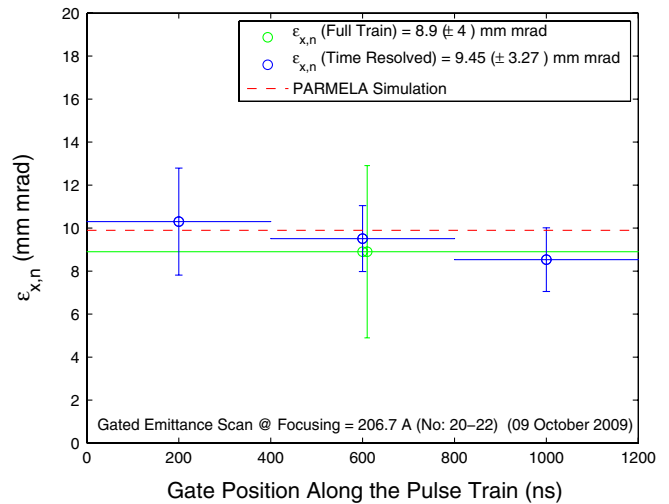

FIG. 12. Emittance measurement along the pulse train with the steps of 400 ns. The charge per bunch and the energy of the beam were 1.6 nC, 4.8 MeV, respectively, during the measurements.

fluctuation of 14.6% along the 1.2 μs bunch train have been recorded.

The emittance behavior follows the rf power fluctuations. This is a systematic behavior of the rf pulse shape which originates from the high voltage (HV) of the klystron. The flattop of the HV pulse which is used at the klystron is not optimized for this particular modulator. The effect of the fluctuations in several parameters has been studied in Ref. [12]. The change in rf power along the train leads to fluctuations in the beam energy, extracted charge, and the phase. According to the simulations the pure rf amplitude variation along the train which is in the level of 1% cannot explain the 15% emittance fluctuation. Nevertheless, the correlation is intriguing therefore a combination of the fluctuations in the above-mentioned parameters could explain the measured emittance fluctuation along the bunch train. Further measurements are needed, in order to sufficiently investigate the mechanism of this correlation.

B. Longitudinal phase space

A 90° magnetic spectrometer was utilized for the energy and the energy spread measurements during the PHIN commissioning. The spectrometer is equipped with an OTR beam profile monitor and a segmented dump in order to observe the momentum distribution of the beam. The former enables the measurements integrated over the bunch train whereas the latter provides the time-resolved information.
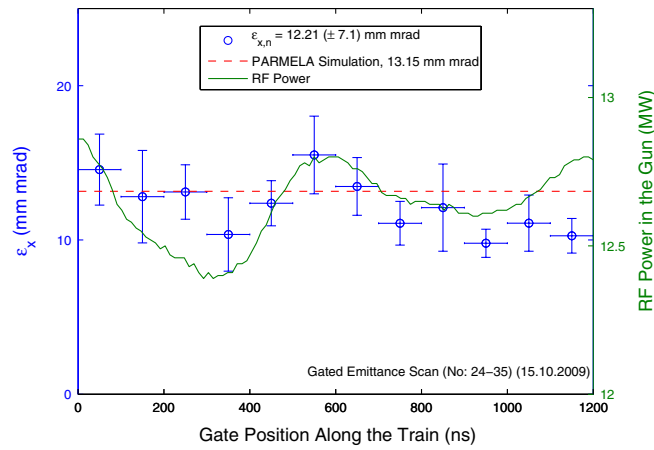
FIG. 13.   The emittance fluctuations along the pulse train in comparison with the rf pulse shape. The measurement has been performed on a beam with the charge of 1 nC per bunch and the energy of 5 MeV.

The OTR profile of a typical PHIN beam in the dispersive section is presented in Fig. 14(a). The OTR profile is analyzed for the horizontal axis which is calibrated in order to retrieve the mean energy and the energy spread of the beam. The energy spread given is the 1σ width of the beam intensity distribution. Consequently, the mean energy has been measured to be 5.43 MeV with a spread of 50 keV as shown in Fig. 14(b).

The segmented dump was designed and implemented in the end of the spectrometer line within the PHIN research program [17]. During the measurements, the pulse train is dumped on the 2 mm-thick isolated stainless steel segments located with a separation of 1 mm. Each segment functions as the Faraday cup. The signals from the 20 individual segments are acquired fast enough enabling a time-resolved monitoring of the beam distribution through 20 channels [18]. The spatial resolution of the device is 4 channels/σ, whereas the time resolution of the device is 10 ns due to the sampling frequency of the analog-to-digital converters used in the setup. With faster sampling channels the system is capable of providing a time resolution of ~500 ps. Figure 15 shows the time-resolved contour plot that belongs to a bunch train of 1300 ns. For this measurement the mean beam energy is 5.97 MeV and the energy spread is 0.73% along the bunch train which is well within the specification of <1%.

The fluctuations in the energy along the bunch train (Fig. 15) can be also correlated with the rf power fluctuations. The comparison of energy fluctuations and the rf power fluctuations in time is presented in Fig. 16.

The stability of the beam parameters along the bunch train has been successfully measured by using the instrumentation developed during the research program. It has been found that further improvements are possible by measuring and optimizing the modulator that results in a flatter rf pulse shape and more stable phase.
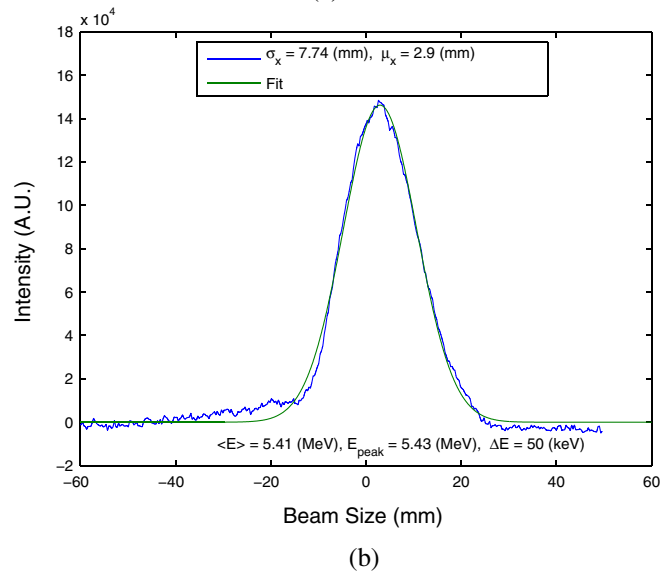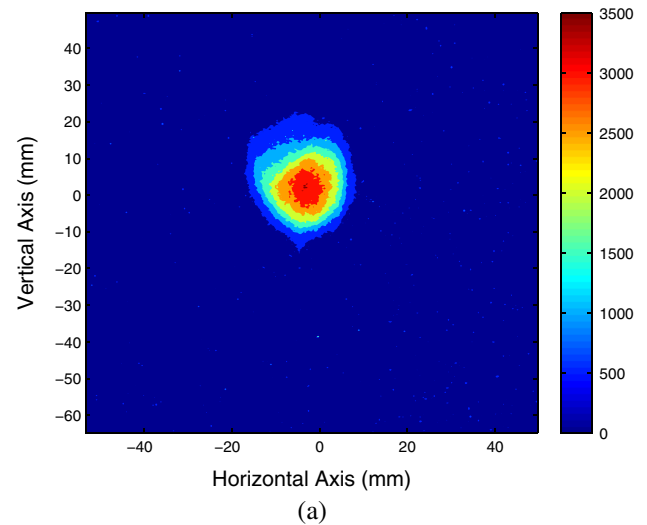

(a)

(b)

FIG. 14.   An example from the energy measurement in the spectrometer by OTR monitoring. (a) The image captured by the CCD camera. (b) The horizontal profile of the image.

C. Beam position and intensity stability

The on-axis position stability of the electron beam is determined mainly by the stability of the laser beam on the cathode. Beam position measurements with the virtual cathode and the OTR camera show a good correlation between the movement of the laser beam and the electron beam as presented in Fig. 17. To further investigate the position instabilities, similar correlation measurements have been carried out between the laser room and the virtual cathode. It has been observed that the stability in the laser room is more than a factor of 3 better than on the diagnostic table beside the photoinjector one floor below. Therefore, a window between the laser room and the machine area has been installed to avoid the air flow. In addition, after the installation of the phase-coding stage, the 10 W preamplifier has been bypassed and a fiber
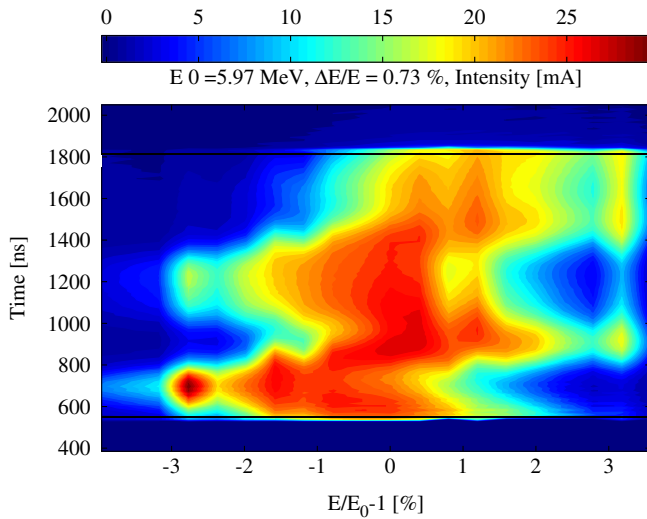
FIG. 15. The time-resolved energy and energy spread measurement by the segmented dump. The contour plot of the energy change during the 1300 ns electron beam hitting the segmented dump.

FIG. 17. The correlation of the position stability between the laser and the electron beam for the horizontal axis.

booster amplifier has been used. Consequently, the beam position instability of 32% (rms) for vertical beam size and 21% for the horizontal beam size were recorded to be improved to 19% and 15%, respectively.

In the future, the pointing stability can be improved by using hard apertures which might be placed on the laser table and fairly close to the cathode (not to collect further instabilities between the aperture and the photocathode) to be imaged on the cathode. In order to use such apertures, the energy margin of the laser should be sufficiently large. Currently, the CLIC requirement for the laser pointing stability has not been specified.
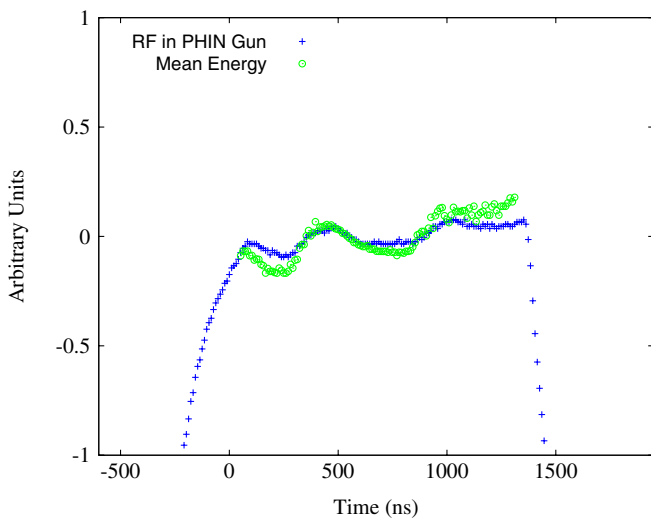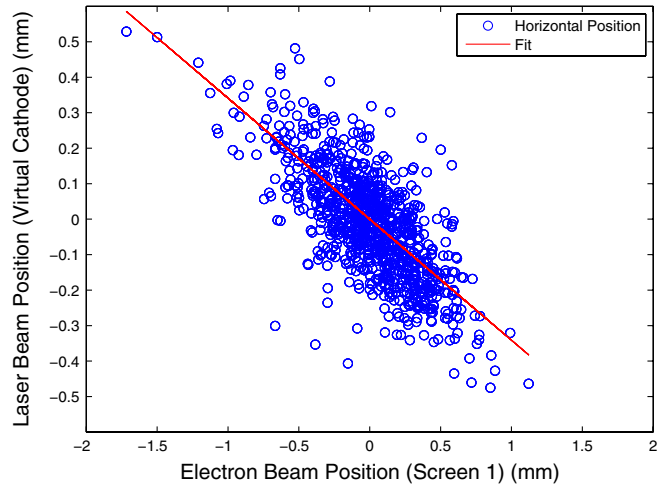
The macropulse amplitude stability measurements for the laser were carried out by viewing the reflection from a viewport and by the integration of a window of interest from the virtual cathode camera. Simultaneously, the charge stability was also recorded by using the beam position monitors and by taking an average value over 10 ns at the beginning of the macropulse. The best and the worst stability values obtained during the experiments are presented in Table III for the nominal PHIN beam of 1.2 μs. The laser is currently running without any active feedback stabilization, only taking advantage of the self-stabilizing feature of the steady-state saturated amplifiers. After the Pockels cell and before the harmonic conversion, a 0.23% (rms) stability in the IR has been measured. This increases to 0.8% (rms) in the green and 1.3% in the UV due to the nonlinear conversion process. Nevertheless, this stability for a high power laser operating in UV is exceptionally good. However, in the conceptual design, CLIC tolerates a drive beam amplitude fluctuation of 0.2%. Therefore, a feedback stabilization system based on electro-optical devices and fast detectors is under development with the aim of reaching the target amplitude stability. Investigation of the bunch to bunch stability is also planned in the future.

FIG. 16. Deviation of the mean energy in correlation with the rf amplitude pulse shape.

TABLE III. The best and the worst measured values for the laser and bunch amplitude stability during the commissioning.

	Laser energy (nJ)	Bunch charge (nC)
Best	369 (1.3%)	1.5 (0.8%)
Worst	330 (2.6%)	1 (2.4%)

VI. CONCLUSIONS AND OUTLOOK

The full characterization of the PHIN photoinjector for the short and the long bunch trains was performed. In order to conduct these experiments a set of diagnostics tools has been utilized which enables both single-shot and time-resolved measurements. Besides the more traditional current monitoring and the OTR profile monitoring techniques, the multislit emittance diagnostics for the space charge dominated beams and the segmented beam dump for the time-resolved energy measurements have been designed and exploited for PHIN beam parameters. Single-shot measurements have been performed to provide shot-to-shot information of the beam, whereas the time-resolved measurements have revealed the beam status along the bunch train. The summary of the experimental results is presented in Table IV. Only the charge stability has been found to be subject to improvement by a factor of 3. The improvement will be done by implementing a feedback stabilization system for the laser intensity on the cathode. The experimental results and the simulations have been compared and found to be in agreement. As a result, the PHIN photoinjector was shown to be an adequate candidate for the CTF3 drive beam electron source. The systems developed within the activity are versatile and can be used at the CLIC parameters in the future, conditionally on the demonstration of the average current for the nominal bunch train length.

One of the technological challenges of a photoinjector for the CLIC drive beam is to produce such a high charge per bunch for the nominal bunch train of 140 μs. The further efforts will be focused on the feasibility study for the production of this exceptionally high average current electron bunch train, based on the findings of the PHIN photoinjector. As the next steps towards the CLIC drive beam source, a phase-coding system has been developed and installed in the existing laser system. The phase-coding setup in the laser consists of a fiber splitter and two arms which houses a variable delay line and a variable attenuator. One of the arms provides a delay of 333 ps whereas the other arm matches the attenuation on the delay line. This is used to manipulate the temporal structure of the beam. Details on the phase-coding system for the PHIN laser can be found in Ref. [19].

The measurements have been performed on both the laser and the electron beam. The fast phase switches with respect to the 1.5 GHz bunch repetition over the 1.2 μs bunch train were achieved. This manipulation of the beam temporal structure is necessary to provide the time structure required by CLIC Test Facility 3 (CTF3). The beam measurements have indicated that the stability of the beam parameters along the train have not been negatively influenced after the introduction of the phase-coding stage. These results can be found in [20].

The general results of the experimental and numerical characterization of the PHIN photoinjector have been used to initiate a photoinjector design with the CLIC drive beam parameters. For this purpose, the PHIN rf gun has been rescaled to provide a 1 GHz resonance frequency at the π mode. Consequently, the preliminary beam dynamics simulations have been performed [21]. Nevertheless, a detailed technical study for the optimization of the rf gun and the further beam dynamics studies should be performed.

TABLE IV. The specifications for the PHIN photoinjector in comparison with the achieved values during the short intermittent runs between 2008–2011.

Parameter	Specification	Achieved
Laser		
UV laser pulse energy (nJ)	370	400
Micropulse repetition rate (GHz)	1.5	1.5
Macropulse repetition rate (Hz)	1–5	1
Train length (ns)	1273	1300
Electron beam		
Charge per bunch (nC)	2.33	8.1@50 ns
		4.4@200 ns
Charge per train (nC)	4446	5800
Bunch length (ps)	8	6.5
Current (A)	3.5	6.6
Transverse normalized emittance (mm mrad)	<25	14
Energy spread (%)	<1	0.7
Energy (MeV)	5.5	5.5
Charge stability (%, rms)	<0.25	0.8
rf gun		
rf gradient (MV/m)	85	85
Quantum efficiency (%)	3	3–18

[1] H. H. Braun, J. P. Delahaye, A. De Roeck, and G. Geschonke, CERN Courier Report No. 35450, 2008 [http://cerncourier.com/cws/article/cern/35450].

[2] M. Battaglia, A. de Roeck, J. Ellis, and D. Schulte (CLIC Physics Working Group), arXiv:hep-ph/0412251; Report No. CERN-2004-005, 2004.

[3] CLIC Collaboration, The Conceptual Design Report of the Compact Linear Collider Project (work in progress).

[4] M. Petrarca, H. H. Braun, E. Chevallay, S. Doebert, K. Elsener, V. Fedosseev, G. Geschonke, R. Losito, A. Masi, O. Mete, L. Rinolfi, A. Dabrowski, M. Divall, N. Champault, G. Bienvenu, M. Jore, B. M. Mercier, C. Prevost, R. Roux, and C. Vicario, Report No. CERN-ATS-2009-134, CLIC-Note-802, 2009.

[5] M. Petrarca, E. Chevallay, S. Doebert, A. Dabrowski, M. Divall, V. Fedoseev, N. Lebas, T. Lefevre, R. Losito, D. Egger, and O. Mete, Report No. CLIC-Note-846, 2010.

[6] M. Divall *et al.*, CARE Report No. 06-021 PHIN.

[7] M. Petrarca, M. Martyanov, M. Csatari Divall, and G. Luchinin, IEEE J. Quantum Electron. **47**, 306 (2011).

[8] R. Roux, G. Bienvenu, and B. Mercier, CARE Report No. Note-2004-034-PHIN, 2004.

[9] Christian Travier, Nucl. Instrum. Methods Phys. Res., Sect. A **340**, 26 (1994).

[10] H. Yamamoto, H. Hamabe, S. Sone, S. Yamaguchi, and M. R. Asakawa, Int. J. Opt. **2011**, 714265 (2011) [http://www.hindawi.com/journals/ijo/2011/714265/].

[11] L. M. Young and J. Billen, in *Proceedings of the 20th Particle Accelerator Conference, Portland, OR, 2003* (IEEE, New York, 2003).

[12] O. Mete, Ph.D. thesis, EPFL, Lausanne, 2011.

[13] O. Mete, E. Chevallay, A. Dabrowski, M. Divall, S. Doebert, D. Egger, K. Elsener, V. Fedosseev, T. Lefevre, and M. Petrarca, Report No. CLIC-Note-809, 2010.

[14] S. G. Anderson *et al.*, Phys. Rev. ST Accel. Beams **5**, 014201 (2002).

[15] B. Carlsten, Nucl. Instrum. Methods Phys. Res., Sect. A **285**, 313 (1989).

[16] Michiko G. Minty and Frank Zimmermann, *Measurement and Control of Charged Particle Beams* (Springer, Berlin, 2003).

[17] D. Egger, A. Dabrowski, and T. Lefevre, Report No. CTF3-Note-099, 2009.

[18] A. Dabrowski, S. Doebert, D. Egger, O. Mete, and T. Lefevre, Report No. CERN-BE-2010-018, 2010.

[19] M. Csatari Divall, A. Andersson, E. Bolzon, B. Bravin, E. Chevallay, A. Dabrowski, S. Doebert, A. Drozdy, D. Egger, V. Fedosseev, C. Hessler, T. Lefevre, S. Livesley, R. Losito, O. Mete, M. Olvegaard, M. Petrarca, and A. N. Rabiller, in *Proceedings of IPAC'11, IPAC'11/EPS-AG* (European Physics Society Accelerator Group, San Sebastian, Spain, 2011), MOPC150.

[20] M. Csatari Divall, A. Andersson, E. Bolzon, B. Bravin, E. Chevallay, A. Dabrowski, S. Doebert, A. Drozdy, D. Egger, V. Fedosseev, C. Hessler, T. Lefevre, S. Livesley, R. Losito, O. Mete, M. Olvegaard, M. Petrarca, and A. N. Rabiller, Nucl. Instrum. Methods Phys. Res., Sect. A **659**, 1 (2011).

[21] O. Mete, CLIC NOTE (work in progress), 2011.